PTEP

Prog. Theor. Exp. Phys. **2021** 123D01(17 pages)
DOI: 10.1093/ptep/ptab136

Single-particle decomposition of nuclear surface diffuseness

Wataru Horiuchi ⋆

Department of Physics, Hokkaido University, Sapporo 060-0810, Japan.
⋆E-mail: whoriuchi@nucl.sci.hokudai.ac.jp

Received August 27, 2021; Revised September 28, 2021; Accepted November 11, 2021; Published November 13, 2021

Nuclear surface diffuseness reflects spectroscopic information near the Fermi level. I propose a way to decompose the surface diffuseness into single-particle (s.p.) contributions in a quantitative manner. Systematic behavior of the surface diffuseness of neutron-rich even–even O, Ca, Ni, Sn, and Pb isotopes is analyzed with a phenomenological mean-field approach. The role of the s.p. wave functions near the Fermi level is explored: The nodeless s.p. orbits form a sharp nuclear surface, while the nodal s.p. orbits contribute to diffusing the nuclear surface.

Subject Index D12, D13

1. Introduction

Studying the structure of short-lived neutron-rich unstable nuclei is one of the most important subjects in nuclear physics. Various exotic phenomena such as halos [1–3] (see also Ref. [4] and references therein), neutron skin [5], and deformation [6,7], have been found through systematic studies of nuclear radii. Since the nuclear radius is sensitive to the nuclear density profile around the nuclear surface, these drastic nuclear structure changes near the Fermi level can be deduced from measurements of the interaction or total reaction cross section. For a deeper understanding of the structure of unstable nuclei predicted by theoretical models, one needs to know more details on the density profiles near the nuclear surface, which may include more information on spectroscopic properties other than the nuclear radius.

To know the whole density distribution, electron scattering has been used to extract the charge distribution of stable nuclei [8]. Combining known charge or proton density distributions, the neutron density distribution has been deduced for some stable nuclei by measuring proton elastic scattering cross sections up to large scattering angles [9,10] (see also Ref. [11] and references therein). The electron scattering [12] and proton elastic scattering [13,14] measurements have been extended for unstable nuclei. However, it is still hard to determine whole density distributions as these require cross-section measurement up to large scattering angles. Even if all the nuclear density distributions cannot be determined, the nuclear surface "diffuseness", which quantifies the nuclear surface thickness, is a promising measure of the surface density profile and can be deduced accurately using nucleus–proton scattering as demonstrated in Ref. [15]. To get the surface diffuseness, one only needs the cross sections at forward angles up to the first peak position, which is advantageous to study unstable nuclei by the inverse kinematics.

Understanding how the surface diffuseness forms is of particular importance as the next-order information on the nuclear radius. Evaluating the surface diffuseness as well as the

neutron skin thickness also impacts on constraining the equation of state of nuclear matter from finite nuclear systems [16–19]. Thus far, various phenomena have been observed that may be closely related to the surface diffuseness: kink structures of total reaction or interaction cross sections in neutron-rich Ne [6] and Mg [7] isotopes due to nuclear deformation [20–25], and core-swelling phenomena in spherical Ca isotopes [26,27]. The surface diffuseness changes at the major or subshell were pointed out in Ref. [15]. A systematic and extensive theoretical study on the surface diffuseness was given in Ref. [28]. Bubble nuclei, which have depleted central density due to the lack of occupation of the *s*-wave orbit, can be identified by measuring the surface diffuseness [29]. The surface diffuseness is drastically enhanced when the *pf* mixed orbits are occupied in the island of inversion in the neutron-rich Ne and Mg isotopes [30].

A density profile near the nuclear surface could mainly be formed by the single-particle (s.p.) wave functions near the Fermi level. The purpose of this paper is to clarify the role of the s.p. wave functions in forming the nuclear surface. I propose a practical and convenient way to decompose the surface diffuseness into each s.p. contribution. As a first step, for simplicity, I only consider spherical configurations generated from a phenomenological mean-field potential.

The paper is organized as follows. Section 2 describes the theoretical models used in this paper. Section 2.1 defines the nuclear surface diffuseness based on a familiar two-parameter Fermi (2pF) density distribution. I derive a relationship between these diffuseness and radius parameters by relating the 2pF density to the one-body density generated from a mean-field model, allowing one to decompose the total surface diffuseness into s.p. contributions. Section 2.2 describes the phenomenological mean-field model employed in this paper. The validity of this approach is confirmed by a comparison of the available experimental data related to nuclear size, i.e., the interaction cross section and charge radius. Section 2.3 shows the total surface diffuseness obtained from the present approach and gives an overview of its general behavior. Section 3 is devoted to a detailed analysis and discusses the role of s.p. orbits in the total surface diffuseness for each isotope. In Sects. 3.1–3.4, results for O, Ca and Ni, Sn, and Pb isotopes are respectively discussed. Section 3.5 explores a global feature of the s.p. wave functions by taking examples of neutron dripline nuclei. The role of the s.p. wave functions near the Fermi level is clarified through an analysis of the radii of the s.p. orbits. Finally, the conclusion is given in Sect. 4.

2. Theoretical models

2.1 *Single-particle decomposition of nuclear surface diffuseness*

To define the nuclear surface diffuseness or thickness parameter, I employ a two-parameter Fermi (2pF) function as an anzatz of the density distribution of a nucleus:

$$\rho_{\rm 2pF}(r) = \frac{\rho_0}{1+\exp\left[(r-R)/a\right]}. \tag{1}$$

For given radius parameter R and diffuseness parameter a, ρ_0 can be determined uniquely by the normalization condition $4\pi\int_0^\infty dr\, r^2 \rho_{\rm 2pF}(r) = A$ with A being the mass number of a nucleus. Expanding the above distribution at R and taking the first-order term, I get

$$\rho_{\rm 2pF}(R) + (r-R)\left.\frac{d\rho_{\rm 2pF}}{dr}\right|_{r=R} = \rho_0\left(\frac{1}{2} - \frac{r-R}{4a}\right). \tag{2}$$

Figure 1 illustrates the geometry of a typical 2pF distribution for ^{208}Pb with the standard parameters $\rho_0 = 0.17$ fm^{-3}, $R = 1.2 \times 208^{1/3}$ fm, and $a = 0.54$ fm [31]. This clearly shows that the diffuseness parameter a corresponds to the slope of the 2pF distribution at the radius

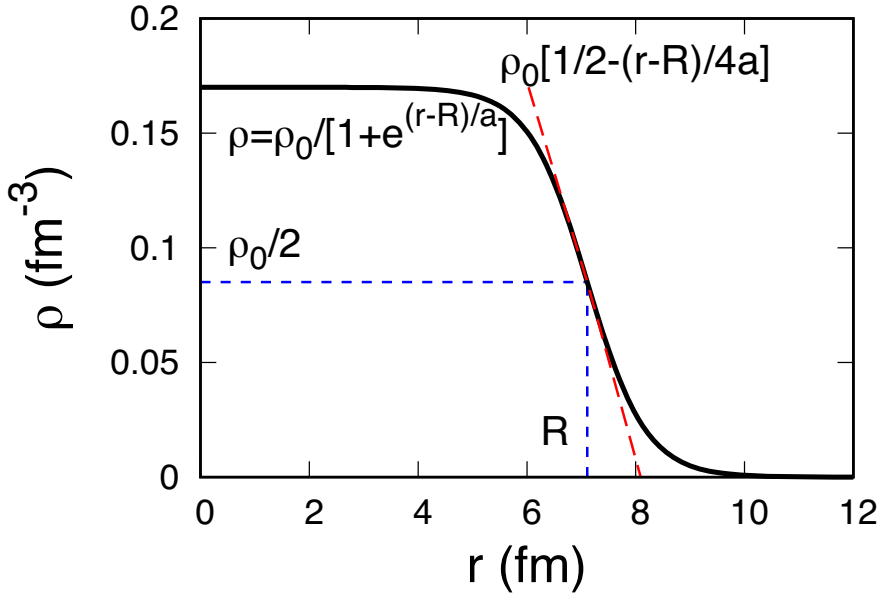

Fig. 1. Geometry of a 2pF density distribution for ^{208}Pb with $\rho_0 = 0.17$ fm^{-3}, $R = 1.2 \times 208^{1/3}$ fm, and $a = 0.54$ fm [31]. The dashed line indicates the slope of the 2pF distribution at the half density ($\rho_0/2$) radius R, which is indicated by the dotted lines.

parameter R, where the 2pF distribution becomes approximately half of the central density $\rho_{\rm 2pF}(0) \approx \rho_0$. This 2pF-type density well approximates typical density distributions [15]. Because of its simplicity, this first-order approximation, which corresponds to a trapezoidal distribution with a surface thickness of $4a$, was applied to correct the sharp nuclear surface of the black-sphere model for high-energy proton–nucleus scattering [32]. I remark that the 2pF distribution may not describe a weakly bound neutron tail. The limitations of this sort of density distribution, especially for halo nuclei, are discussed in Ref. [33].

Decomposition of the nuclear density distribution can be made by assuming that the total density is composed of a sum of single-particle (s.p.) density distributions $\bar{\rho}_i$ as

$$\rho(r) = \sum_{i=1}^{A} \bar{\rho}_i(r). \tag{3}$$

Given the relationships of Eqs. (1) and (2), it is straightforward to decompose the surface diffuseness parameter into each s.p. contribution. Differentiating this density of Eq. (3) at $r = R$, I get a relation by assuming $\rho(r) = \rho_{\rm 2pF}(r)$:

$$\left.\frac{d\rho}{dr}\right|_{r=R} = \sum_{i=1}^{A} D_i = -\frac{\rho_0}{4a} \tag{4}$$

with

$$D_i = \left.\frac{d\bar{\rho}_i}{dr}\right|_{r=R}. \tag{5}$$

Finally, the surface diffuseness is expressed by

$$a = -\frac{\rho_0}{4}\left(\sum_{i=1}^{A} D_i\right)^{-1}. \tag{6}$$

The diffuseness parameter a is inversely proportional to the sum of D_i. To evaluate D_i, the R value should be defined for general density distributions. As shown later, the a value can reasonably be obtained with a proper choice of R. I will investigate these D_i values for each s.p. density distribution and quantify the s.p. contribution to the total surface diffuseness a.

2.2 *Density distributions of O, Ca, Ni, Sn, and Pb isotopes*

In this paper, I generate the s.p. density distributions $\bar{\rho}_i$ from a phenomenological mean-field model [31] for the sake of simplicity. The mean-field potential is parameterized as

$$V(r) = V_0 f(r) + V_1(\boldsymbol{l}\cdot\boldsymbol{s})r_0^2\frac{1}{r}\frac{df}{dr} + V_C(r)\frac{1}{2}(1-\tau_3) \tag{7}$$

with the Woods–Saxon form factor, $f(r) = \{1+\exp[(r-R_{\rm WS})/a_{\rm WS}]\}^{-1}$, and

$$V_0 = -51 + 33\frac{N-Z}{A}\tau_3, \quad V_1 = 22 - 14\frac{N-Z}{A}\tau_3 \tag{8}$$

in units of MeV, with N and Z being the neutron and proton numbers, respectively, and $\tau_3 = \pm 1$ corresponding to $+$ $(-)$ for the neutron (proton). The radius and diffuseness parameters of the potential are given respectively by $R_{\rm WS} = 1.27A^{1/3}$ fm and $a_{\rm WS} = 0.67$ fm. The Coulomb potential term V_C is taken as a uniform charge distribution with radius $R_{\rm WS}$. I calculate all s.p. bound states and obtain their radial s.p. wave functions $\psi_{nlj}(r)$ with n, l, j being radial, orbital, and angular momentum quantum numbers, respectively. By averaging over magnetic quantum numbers and integrating over the spin coordinate, the density distributions are expressed by a sum of squared radial s.p. wave functions, in which the outermost s.p. level is averaged and filled equally as

$$\rho(r) = \sum_{n,l,j\in{\rm occ.}}(2j+1)|\psi_{nlj}(r)|^2 + N_v|\psi_{n_vl_vj_v}(r)|^2 \tag{9}$$

with $4\pi\int_0^\infty dr\, r^2|\psi_{nlj}(r)|^2 = 1$ and $4\pi\int_0^\infty dr\, r^2\rho(r) = A$, where N_v is the number of the outermost nucleon with the quantum numbers n_v, l_v, and j_v. Note that $\bar{\rho}_i$ in Eq. (3) is nothing but $|\psi_{nlj}|^2$. The root-mean-square (rms) radius of each s.p. orbit can be evaluated by

$$r_{nlj} = \sqrt{4\pi\int_0^\infty dr\, r^4|\psi_{nlj}(r)|^2} \tag{10}$$

and the rms matter radius is given by

$$R_m = \sqrt{\frac{4\pi}{A}\int_0^\infty dr\, r^4\rho(r)}. \tag{11}$$

I calculate such density distributions for proton magic nuclei for O, Ca, Ni, Sn, and Pb isotopes. Since the parameter set of Ref. [31] was determined to reproduce the properties of medium- to heavy-mass nuclei, this parameter set may not be appropriate to describe light nuclei such O isotopes [34,35]. In fact, the neutron dripline of O isotopes is predicted at ^{28}O, which contradicts the measurements [36–38]. Therefore, I modify the potential parameter for O isotopes as $R_{\rm WS} = 1.20A^{1/3}$ fm and $a_{\rm WS} = 0.60$ fm to reproduce the neutron dripline ^{24}O. For the other isotopes, I use the original parameter sets as they are. Finally, I find even–even isotopes, $^{14\text{–}24}$O, $^{34\text{–}60}$Ca, $^{50\text{–}86}$Ni, $^{96\text{–}164}$Sn, and $^{178\text{–}266}$Pb. I remark that some exotic nuclear structure was predicted in the neutron-rich Ca isotopes for $N > 40$ that must be reflected in the surface diffuseness [39–42]; however, this parameter set does not produce a bound $0g_{9/2}$ orbit for $N > 40$. A detailed study along the isotopic chain beyond $N = 40$ using a more realistic structure model is quite interesting and will be reported elsewhere.

Table 1. Calculated rms matter radii and comparison of calculated total reaction and experimental interaction cross sections of O and Ca isotopes on a carbon target. The cross sections are computed at 1000 and 300 MeV/nucleon for the O and Ca isotopes, respectively. Experimental data are taken from Refs. [26,51,52].

	R_m (fm)	σ_R (mb)	σ_I(Expt.) (mb)
^{16}O	2.55	980	982 ± 6
^{18}O	2.69	1060	1032 ± 26
^{20}O	2.83	1140	1078 ± 10
^{22}O	2.95	1210	1172 ± 22
^{24}O	3.22	1370	1318 ± 52
^{42}Ca	3.40	1430	$1463 \pm 13 \pm 6$
^{44}Ca	3.46	1460	$1503 \pm 12 \pm 6$
^{46}Ca	3.51	1500	$1505 \pm 9 \pm 6$
^{48}Ca	3.57	1540	$1498 \pm 17 \pm 6$
^{50}Ca	3.65	1600	$1615 \pm 42 \pm 7$

To evaluate the validity of the calculated density distributions, the nuclear radii are useful observables as they properly reflect the density profile near the nuclear surface. First, I calculate the total reaction cross section at high incident energy, which directly reflects the matter density profile. The nucleon-target profile functions [43] in the Glauber model [44] are employed, allowing us to get reliable total reaction cross sections of high-energy nucleus–nucleus collisions. Inputs of the model are the density distributions of the projectile and target nuclei, and the so-called profile function, which describes nucleon–nucleon scattering. The parameter of the profile function is taken from Ref. [45]. This model nicely describes the total reaction cross sections at high incident energies. See Refs. [23,25,46–50] for various applications.

Table 1 compares the calculated total reaction and experimental interaction cross-section data on a carbon target at high incident energies, 1000 MeV/nucleon for O isotopes and 300 MeV/nucleon for Ca isotopes. Good agreement for all listed O and Ca isotopes including the recent cross-section data for neutron-rich Ca isotopes [26] is attained. The calculated rms matter radii are also consistent with those obtained in Refs. [26,51,52]. In addition to the cross-section data, I also compare in Fig. 2 the rms point-proton radii of O, Ca, Ni, Sn, and Pb isotopes evaluated by $R_p = \sqrt{\frac{4\pi}{Z}\int_0^\infty dr\, r^4 \rho_p(r)}$, where $\rho_p(r)$ is the proton density. The "experimental" point-proton radii are extracted from experimental charge radii [53,54]. Overall agreement with the theory and experimental data is obtained, and thus the density distributions employed in this paper reasonably describe the density profile near the nuclear surface.

2.3 *Evaluation of surface diffuseness from single-particle densities*

I have confirmed that the calculated density distributions reasonably reproduce the existing experimental data related to the nuclear size. In this subsection, I extract the diffuseness parameter a from those density distributions by using the relation of Eq. (6) with the reference radius parameter R. As was demonstrated in Ref. [15], the nuclear density distribution ρ is well approximated by the 2pF distribution $\rho_{\rm 2pF}$ with the nuclear radius R and diffuseness a parameters being fixed by minimizing

$$\int_0^\infty dr\, r^2 |\rho(r) - \rho_{\rm 2pF}(r)|. \tag{12}$$

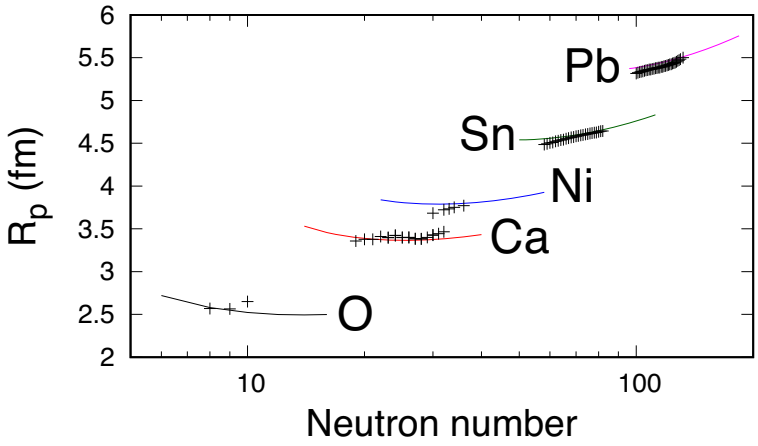

Fig. 2. The rms point-proton radii of even–even O, Ca, Ni, Sn, and Pb isotopes as a function of neutron number. The experimental point-proton radii, which are indicated by plus symbols, are extracted from the experimental charge radii [53,54].

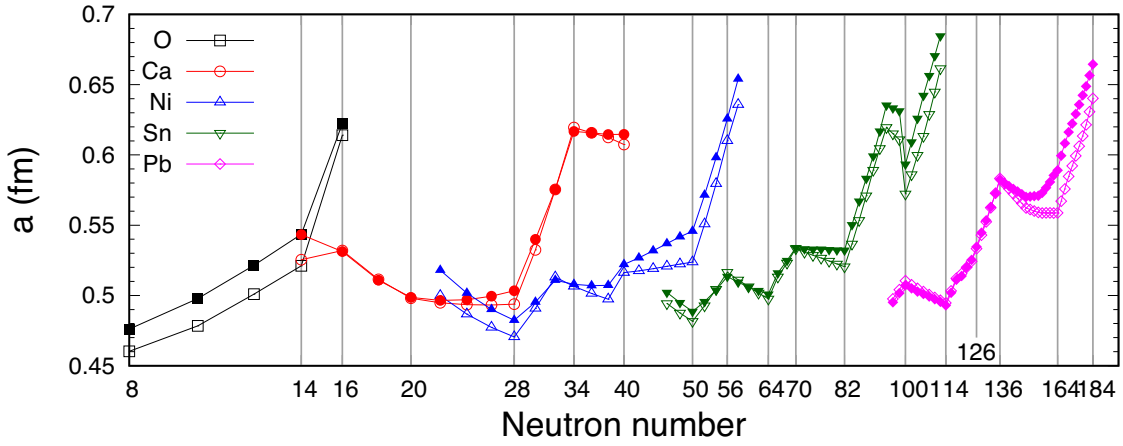

Fig. 3. Diffuseness parameters of even–even O, Ca, Ni, Sn, and Pb isotopes evaluated from Eq. (6) as a function of neutron number. Closed symbols denote those obtained with the minimization of Eq. (12). Thin lines connecting symbols are a guide to the eye. Note that the neutron number is given in logarithmic scale and some magic and semi-magic numbers are indicated by thin vertical lines.

With this prescription, the 2pF distribution nicely reproduces the density profile near the nuclear surface obtained from realistic mean-field calculations including nuclear pairing and deformation [15]. One can obtain the total diffuseness a of Eq. (6) by taking the differentiation of $\bar{\rho}_i$ at R. I note that the radius parameter R in the 2pF distribution of Eq. (1) is in general different from the rms matter radius R_m defined in Eq. (11). An approximate relationship up to the second order of $(a/R)^2$ is given as [31]

$$R_m^2 \approx \frac{3}{5}R^2\left[1+\frac{7}{3}\pi^2\left(\frac{a}{R}\right)^2+\cdots\right]. \tag{13}$$

Apparently, $R_m = \sqrt{3/5}R$ holds if $a = 0$ (sharp-cut radius) and the nuclear diffuseness parameter a works to enhance the nuclear radius R_m from the reference radius of the 2pF density R.

Figure 3 compares those a values obtained using Eqs. (6) and (12). It should be noted that the relation of Eq. (6) is exact if the density distribution is the 2pF function but in general it deviates from that. Nevertheless, the a values obtained from Eq. (6) are found to be close to the

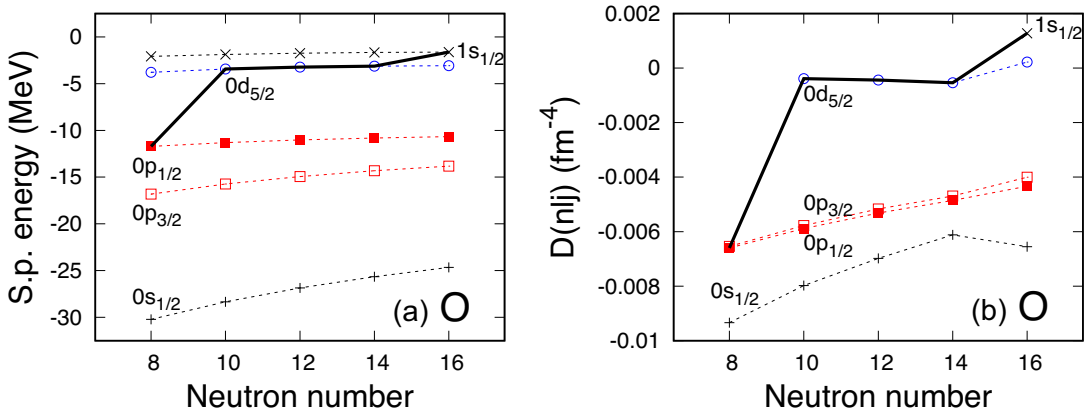

Fig. 4. (a) Neutron single-particle (s.p.) energies and (b) derivative of the s.p. density at the radius parameter R for O isotopes. Thick black lines indicate the Fermi level, where the outermost neutrons are occupied. Plus and cross symbols indicate the $0s_{1/2}$ and $1s_{1/2}$ orbits, respectively. Squares and circles indicate the p and d orbits, respectively. Open and closed symbols distinguish the j-upper ($j_> = l + 1/2$) and j-lower ($j_< = l - 1/2$) orbits, respectively. Thin dotted lines are a guide to the eye.

values obtained with Eq. (12): The deviation is at most 0.03 fm and the square root of the rms deviation between these diffuseness parameters is 0.014 fm for all isotopes adopted in this paper. This means that the surface regions of those density distributions are well approximated by the 2pF distribution, and thus it makes sense to decompose the diffuseness parameters into the s.p. contributions using the relation of Eq. (6). In the following section, I discuss the contribution of the s.p. orbit on the surface diffuseness in detail.

The averaged a value is found to be 0.54 fm, which is consistent with the empirical one [31,55]. Even though the phenomenological Woods–Saxon parameter assumes a constant $a_{\rm WS}$ value, a variety of a values for the density distributions are obtained: some kink structures at the magic and semi-magic numbers, reflecting their s.p. density compositions. Detailed discussions will be given in the next section. This paper aims to clarify the role of the s.p. wave function in the total surface diffuseness. I note, however, that for more realistic cases the pairing interaction gives a smooth transition of the diffuseness parameter across the magic numbers [15,19,33]. Some kink structures disappear owing to the mixing of the s.p. levels near the Fermi level. A detailed study with the pairing interaction would be interesting and is worth studying in future as an extension of this study.

3. Results and discussion

3.1 *O isotopes*

Figure 4(a) displays the neutron s.p. energies of $^{16-24}$O as a function of neutron number. For a guide to the eye, a thick black line indicates the Fermi level, where the outermost neutrons are occupied. As seen in Fig. 3, ^{16}O has the smallest diffuseness parameter among all the isotopes due to well bound p orbits. By filling neutrons in the $0d_{5/2}$ orbit near the Fermi level for $N > 8$, the surface diffuseness gradually increases to $N = 14$. Finally, a sudden increase of the surface diffuseness is obtained due to the occupation of the $1s_{1/2}$ orbit at $N = 16$.

This behavior can be quantified and properly reflected in the derivative of the s.p. orbit at the radius parameter R, i.e., D_i of Eq. (5). For the sake of convenience, hereafter the label of nucleon i is denoted by the quantum numbers of the s.p. wave function nlj, e.g., D_i as $D(nlj)$.

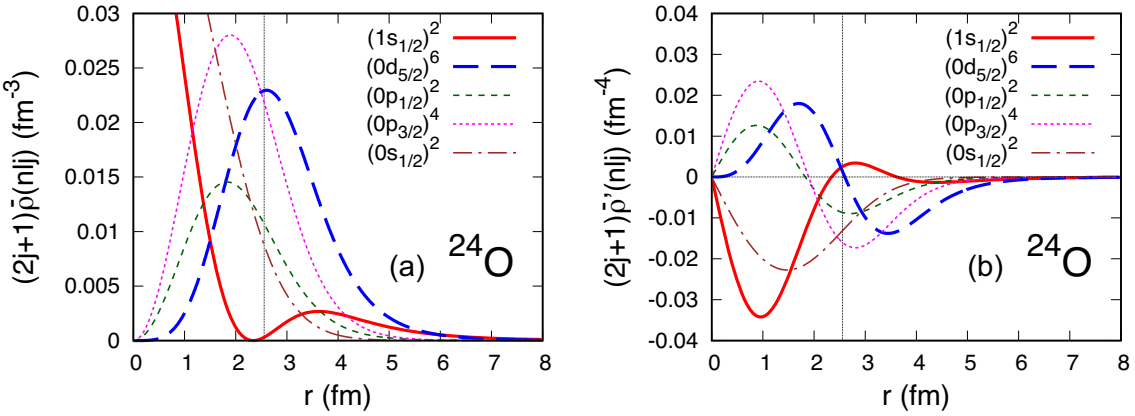

Fig. 5. (a) Neutron single-particle densities and (b) their derivative of ^{24}O multiplied by the occupation number $(2j+1)$. Vertical lines indicate the radius parameter $R = 2.56$ fm of ^{24}O and the horizontal line indicates zero.

Figure 4(b) plots the calculated $D(nlj)$ values of each neutron s.p. orbit. The values are negative for deeply bound $0s_{1/2}$, $0p_{3/2}$, and $0p_{1/2}$ orbits, forming a sharper nuclear surface of ^{16}O ($N = 8$), $a = 0.460$ fm, compared to the standard value 0.54 fm [31]. The $D(nlj)$ values for the $0d_{5/2}$ orbit are almost zero. This means that this s.p. orbit does not explicitly contribute to changing the diffuseness parameter for $^{18-22}$O ($N = 10$–14), even though the $0d_{5/2}$ orbit has the largest orbital angular momentum in O isotopes. For ^{24}O ($N = 16$), since the $1s_{1/2}$ orbit has a positive $D(nlj)$ value, the last two neutrons play a role in enhancing the surface diffuseness.

To understand the behavior of $D(nlj)$ intuitively, Figs. 5(a) and (b) respectively show the neutron s.p. densities $\bar{\rho}(nlj)$ and their derivatives $d\bar{\rho}(nlj)/dr = \bar{\rho}'(nlj)$ of ^{24}O. Each s.p. density is multiplied by the number of occupied neutrons. The radius parameter R of ^{24}O is indicated as a vertical line in the plot. For the deeply bound orbits with $0s_{1/2}$, $0p_{3/2}$, and $0p_{1/2}$, the radius R is located beyond these peak positions as illustrated in Fig. 5(a). These $D(nlj)$ values are negative, which can be seen quantitatively in Fig. 5(b). For $0d_{5/2}$ orbits, the R value is located around the peak position and thus the $D(nlj)$ value is almost zero. A striking difference among the other orbits is found in the $1s_{1/2}$ orbit. Because the $1s_{1/2}$ orbit has a node and is further extended than the other orbits, the R position is located uphill towards the second peak of the s.p. density, leading to a positive $D(nlj)$ value.

The global behavior of the s.p. contribution can also be understood from Figs. 5(a) and (b). As seen in Fig. 4(b), the absolute value of $D(nlj)$ for the deeply bound states gradually increases because the radius parameter R grows with increasing N. Even though the "valence" $0d_{5/2}$ orbit does not explicitly contribute to changing the surface diffuseness, a moderate increase in the surface diffuseness is found in $N = 10$–14. This is mainly due to the change in the nuclear surface defined by the radius parameter R. Since the nuclear surface becomes further from the surface of the "core" with increasing N, in general, as expected from Fig. 4(b), the s.p. orbits in the core, i.e., $0s_{1/2}$, $0p_{3/2}$, and $0p_{1/2}$, orbits, contribute to enhancing the diffuseness parameter a. The properties of the valence neutron orbits are essential to explain the evolution of the surface diffuseness. Since the $1s_{1/2}$ orbit is extended and enhances the nuclear matter radius drastically by 0.27 fm from ^{22}O, which is about twice the enhancement in $N = 10$–14, the diffuseness a and the radius parameter R are changed significantly at $N = 16$, producing kinks in the $D(nlj)$ values for the other s.p. orbits.

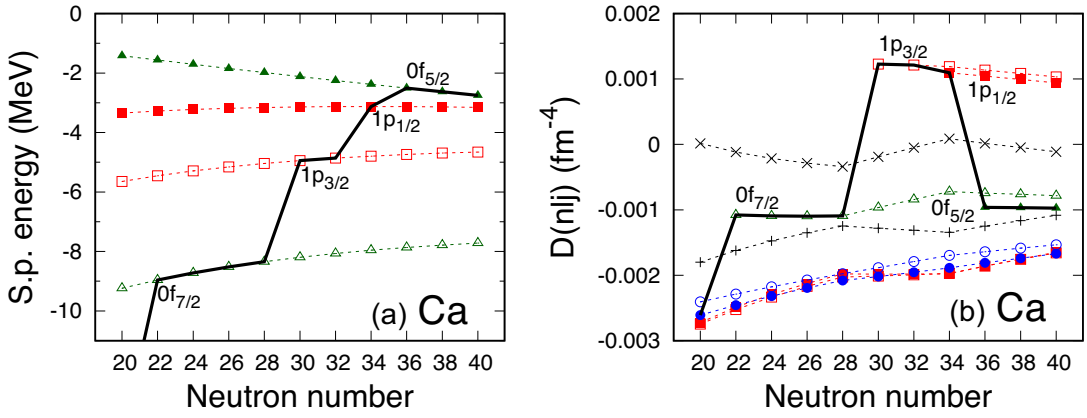

Fig. 6. Same as Fig. 4 but for Ca isotopes. Only s.p. energies near the Fermi level are shown. Triangles indicate the f orbit.

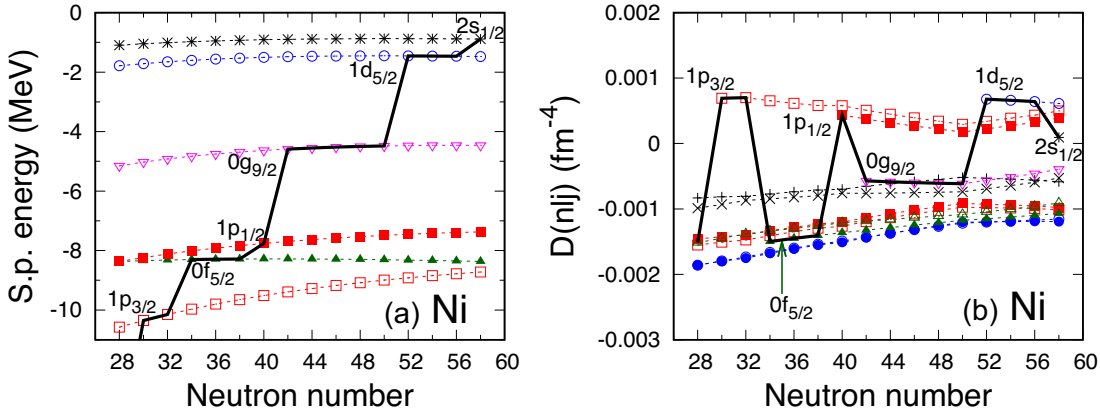

Fig. 7. Same as Figs. 4 and 6 but for Ni isotopes. Only s.p. energies near the Fermi level are shown. Inverted triangles and star symbols indicate the g and $2s_{1/2}$ orbits, respectively.

3.2 *Ca and Ni isotopes*

Figures 6 and 7 display the neutron s.p. energies and $D(nlj)$ values of Ca and Ni isotopes as a function of the neutron number. Compared to the O isotopes, which mainly consist of the nuclear surface, the absolute value of each $D(nlj)$ becomes smaller and the N dependence becomes weaker. Since the surface diffuseness consists of the sum of each s.p. contribution, the weight of each s.p. contribution to the total surface diffuseness becomes smaller for medium-mass nuclei compared to light nuclei. The isotope dependence of the surface diffuseness can easily be understood by considering the role of the "core" and "valence" neutrons. For Ca and Ni isotopes, the core orbits, i.e., all the s.p. orbits below $N = 20$ and 28, respectively, give similar $D(nlj)$ values due to deep binding and contribute to gradually enhancing the surface diffuseness as overall behavior[1], while the valence neutron orbits determine the evolution of the surface diffuseness, depending on their quantum numbers.

[1]At a closer look, like the case of $0d_{5/2}$ of ^{24}O in Fig. 5, the $D(nlj)$ value of the $1s_{1/2}$ orbit in Ca isotopes is almost zero, where the nuclear radius R is located around the second peak of the s.p. density. For Ni isotopes, since the $1s_{1/2}$ orbit is deeply bound and the radius parameter R is larger than that of the Ca isotopes, the R value becomes located beyond the second peak of the s.p. density.

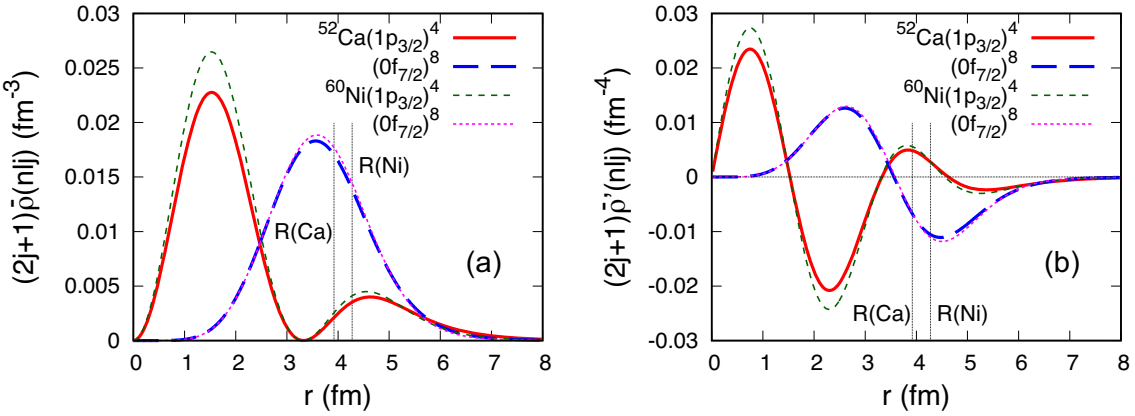

Fig. 8. Same as Fig. 5 but for ^{52}Ca and ^{60}Ni. Single-particle states near the Fermi levels are selected. Vertical lines indicate the radius parameters, $R(\mathrm{Ca}) = 3.92$ fm for ^{52}Ca and $R(\mathrm{Ni}) = 4.27$ fm for ^{60}Ni.

Filling of the lower-l or nodal orbit near the Fermi level produces larger surface diffuseness owing to a smaller centrifugal barrier. In fact, as seen in Fig. 3 for Ca isotopes, the diffuseness parameter at $N = 20$–28 shows constant behavior with relatively small diffuseness $\approx$0.5 fm because of the filling of the $0f_{7/2}$ orbit. A sudden increase in the surface diffuseness occurs at $N > 28$ due to the occupation of the $1p$ orbits, which is consistent with the implication from the recent interaction cross-section measurement [26] and theoretical interpretation [27]. The surface diffuseness stops growing due to the occupation of the $0f_{5/2}$ orbit at $34 < N \leq 40$.

For Ni isotopes, in contrast to the case of the Ca isotopes, no drastic increase in the surface diffuseness is found at $N > 28$. In $28 < N < 40$, three sorts of s.p. orbits are filled in the order of $1p_{3/2}$, $0f_{5/2}$, and $1p_{1/2}$. This change in the filling orbit corresponds to the kinks at $N = 32$ and 38. For the same N, the surface diffuseness is smaller than the Ca isotopes. The reason for this can be seen in Fig. 7, which draws the neutron s.p. energies and $D(nlj)$ of Ni isotopes. The $D(nlj)$ values of the $1p$ orbits are smaller than those of the Ca isotopes. This is partly because the $1p$ orbits are shrunken due to deeper binding of the s.p. orbits in Ni isotopes and partly because the radius parameter R with the same N is larger than that of Ca. Figure 8 plots the s.p. neutron densities and their derivatives near the Fermi levels, i.e., $0f_{7/2}$ and $1p_{3/2}$ of ^{52}Ca and ^{60}Ni. The s.p. wave functions are shrunken, especially for the $1p_{3/2}$ orbit of ^{60}Ni compared to that of ^{52}Ca. The rms radius of the $0f_{7/2}$ and $1p_{3/2}$ orbits of ^{52}Ca (^{60}Ni) are 4.33 (4.26) and 4.76 (4.35) fm, respectively. In addition to the shrinkage of the s.p. wave function, the radius parameter R is also larger for ^{60}Ni. Consequently, the nuclear surface of ^{60}Ni becomes sharper than ^{52}Ca. As seen in Figs. 6(b) and 7(b), the nodal $1p$ orbit always gives a positive $D(nlj)$ value for Ni and Ca isotopes because the radius parameter R is always located before the second peak of the s.p. density as displayed in Fig. 8.

I remark that similar enhancement of the surface diffuseness has been found in neutron-rich Ne and Mg isotopes [30]. Interestingly, this occurs earlier than $N = 28$ but $N > 18$ in the so-called island of inversion, where strong nuclear deformation is found. Nuclear deformation allows the occupation of the intruder orbit, which induces configuration mixing of the spherical $0f_{7/2}$ and $1p$ orbits. Since the mixing includes the low-l $1p$ orbits, the surface diffuseness is drastically enhanced, while the $0f_{7/2}$ mixing forms a sharper surface diffuseness. This exemplifies that the discussion given in this paper remains general for such deformed nuclei.

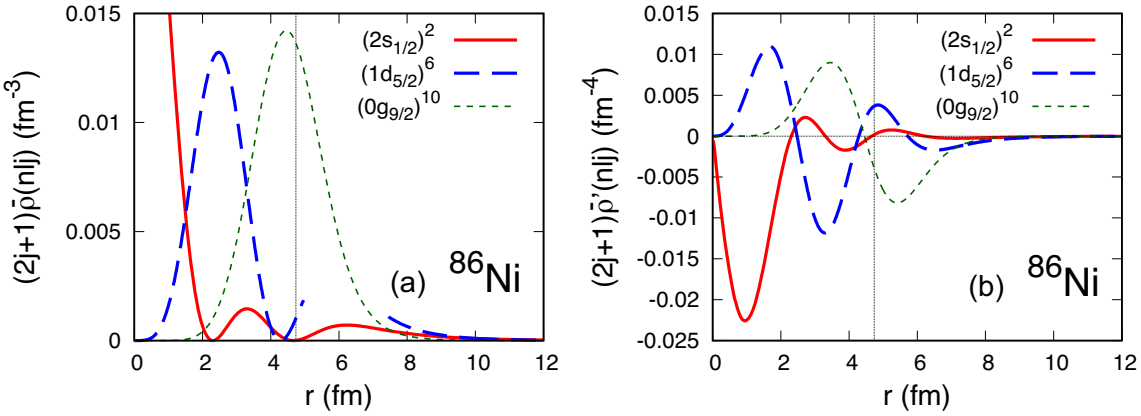

Fig. 9. Same as Fig. 8 but for ^{86}Ni. Vertical lines indicate the radius parameter $R = 4.74$ fm.

Nuclear deformation in general induces fractional occupation numbers near the Fermi level, which may include lower-l orbits, leading to larger surface diffuseness [56].

A sudden increase in the surface diffuseness occurs at $N > 50$ after "sharp" $0g_{9/2}$ orbits are fully occupied for Ni isotopes due to the occupation of the lower-l orbits, $2s_{1/2}$ and $1d_{5/2}$. For ^{86}Ni, as seen in Fig. 7(b), the nuclear surface is diffused mostly by the filling of the $1d_{5/2}$ orbits. Figure 9 plots these s.p. densities and their derivatives for ^{86}Ni. The radius parameter R is located inside the second and third peaks for $1d_{5/2}$ and $2s_{1/2}$ orbits, respectively, giving positive $D(nlj)$ values, while the nodeless $0g_{9/2}$ orbit gives a negative derivative of the s.p. density at the radius parameter R because the R value is located just after the peak of the s.p. density. Note that in Fig. 7(b) the $D(nlj)$ value of the $2s_{1/2}$ orbit is smaller than that of the $1d_{5/2}$ orbit, which has higher angular momentum. This is partly because the s wave has no centrifugal barrier and thus a smaller derivative of the s.p. density in the nuclear surface region is in general obtained compared to $1d_{5/2}$ orbit, and partly because the R value is accidentally located in the second dip of the s.p. density. For this ^{86}Ni case, although the $2s_{1/2}$ orbit does not contribute to changing the diffuseness parameter, it plays a role in forming a halo tail as the s.p. energy is small, -0.888 MeV, resulting in the rms s.p. radius 7.60 fm, which is much larger than the matter radius of ^{86}Ni, 4.56 fm.

3.3 *Sn isotopes*

As shown in Fig. 3 for Sn isotopes, no strong enhancement of the surface diffuseness occurs in $50 < N < 56$. This can be understood by the same reason found in the comparison of Ca and Ni isotopes in $28 < N < 40$. At $N = 50$–70, the $1d_{5/2}$, $0g_{7/2}$, $1d_{3/2}$, and $2s_{1/2}$ orbits, which belong to the principal quantum number $q = 2n + l = 4$, are contributed and change the surface diffuseness: The nodal s.p. orbit diffuses the nuclear surface, while the nodeless s.p. orbit sharpens it. At $N = 70$–82, the reduction of the surface diffuseness is due to the occupation of the $0h_{11/2}$ orbit ($q = 5$).

Figure 10 plots the s.p. energies and $D(nlj)$ values for $N > 80$. A sudden increase in the surface diffuseness $N > 82$ is due to the occupation of the nodal $1f_{7/2}$ orbit ($q = 5$). Level inversions of the low-l $2p_{3/2}$ and sharp $0h_{9/2}$ orbits occur, producing the wiggles at $N \approx 94$–100. It is again noted that, in reality, these kink structures disappear because those s.p. orbits are mixed by the pairing correlation [15], which induces fractional occupation of the orbits near the Fermi level. At $N > 100$, strong enhancement of the surface diffuseness is found. Regarding ^{150}Sn as a core

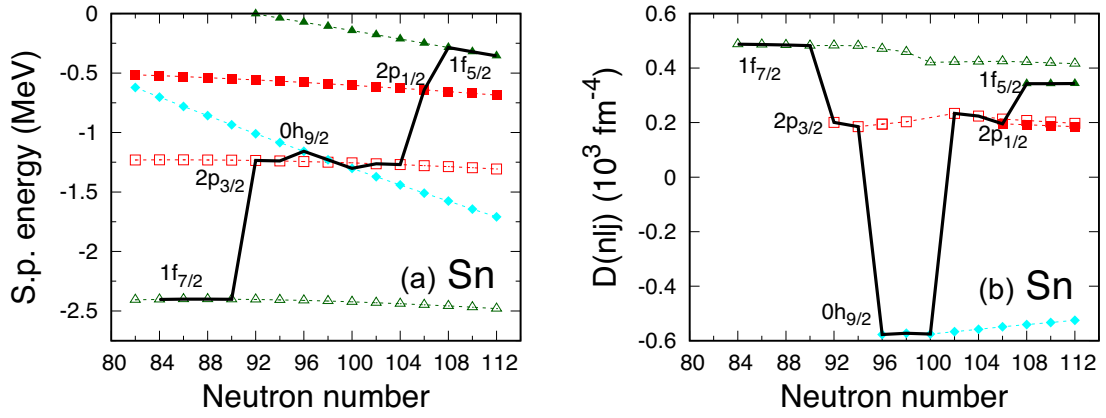

Fig. 10. Same as Figs. 4,6, and 7 but for Sn isotopes. Only s.p. energies near the Fermi level and corresponding $D(nlj)$ values are shown. Closed diamonds indicate the $0h_{9/2}$ ($l = 5$) orbit. Note that the $D(nlj)$ values are multiplied by 10^3 for the sake of convenience.

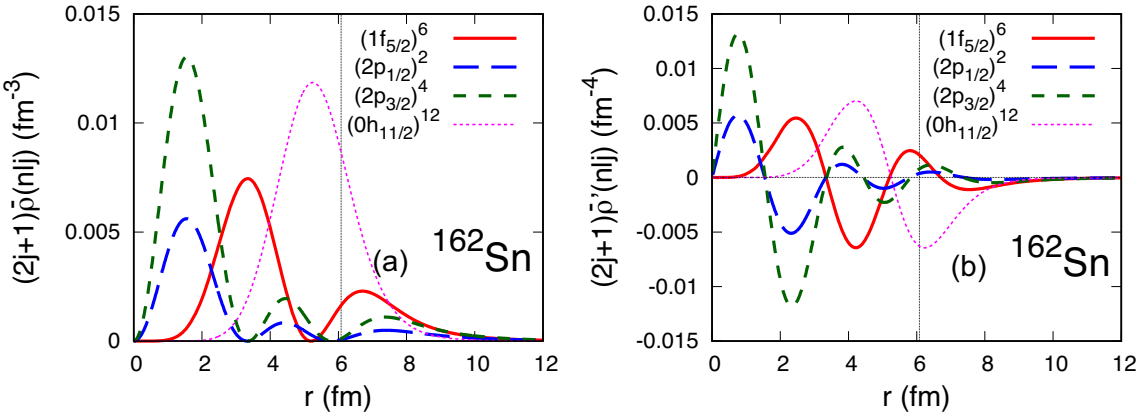

Fig. 11. Same as Fig. 8 but for ^{162}Sn. Vertical lines indicate the radius parameter $R = 6.08$ fm.

nucleus, all the nodal valence orbits with $1f_{7/2}$, $2p_{3/2}$, $2p_{1/2}$, and $1f_{5/2}$, have positive $D(nlj)$ values and contribute to increasing the surface diffuseness. Figure 11 displays the s.p. densities and their derivatives of ^{162}Sn. While the outermost core orbit $0h_{11/2}$ gives a negative $D(nlj)$ value, all these nodal s.p. orbits show positive $D(nlj)$ values that form the diffused nuclear surface. The higher the l value, the larger the magnitude of the $D(nlj)$ value becomes because the variation of the s.p. density near the nuclear surface becomes large for the high-l state.

3.4 *Pb isotopes*

Finally, I discuss Pb isotopes. As seen in Fig. 3, I find apparent kink behavior at the neutron magic numbers, where the nuclear major or subshell is fully occupied. However, $N = 126$ is one exception in that no prominent kink behavior is found even though the major shell is fully occupied. I remark that a similar result has already been shown in Ref. [15]. Figure 12 plots the neutron s.p. energies and $D(nlj)$ values of Pb isotopes. At $114 < N \leq 126$ the surface diffuseness grows by filling neutrons in $2p$ and $1f_{5/2}$ orbits ($q = 5$). For $N > 126$, the major shell is changed to $q = 6$; however, the nodal $1g_{9/2}$ orbit, which has a positive $D(nlj)$ value, leads to a further increase in the surface diffuseness and thus the kink structure disappears.

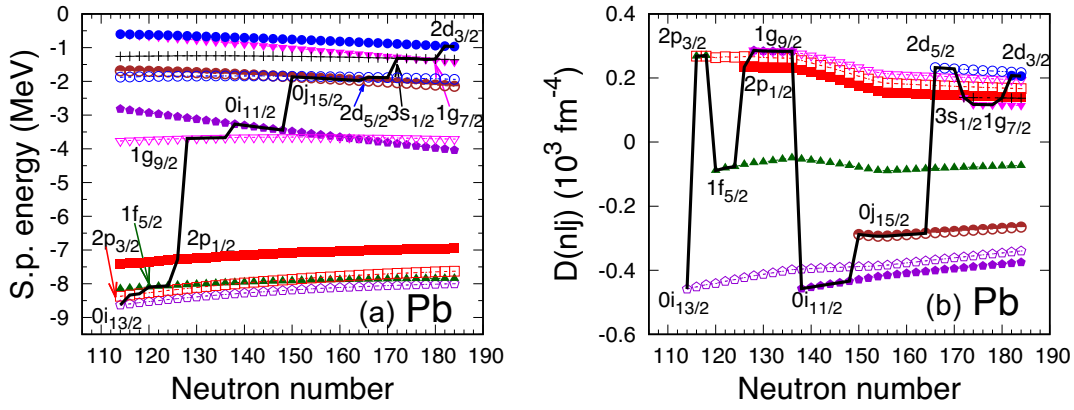

Fig. 12. Same as Figs. 4,6,7, and 10 but for Pb isotopes. Pentagons, half-open circles, and plus symbols indicate the $0i$ ($l = 6$), $0j_{15/2}$ ($l = 7$), and $3s_{1/2}$ orbits, respectively. Only s.p. energies near the Fermi level and corresponding $D(nlj)$ values are shown. Note that the $D(nlj)$ values are multiplied by 10^3 for the sake of convenience.

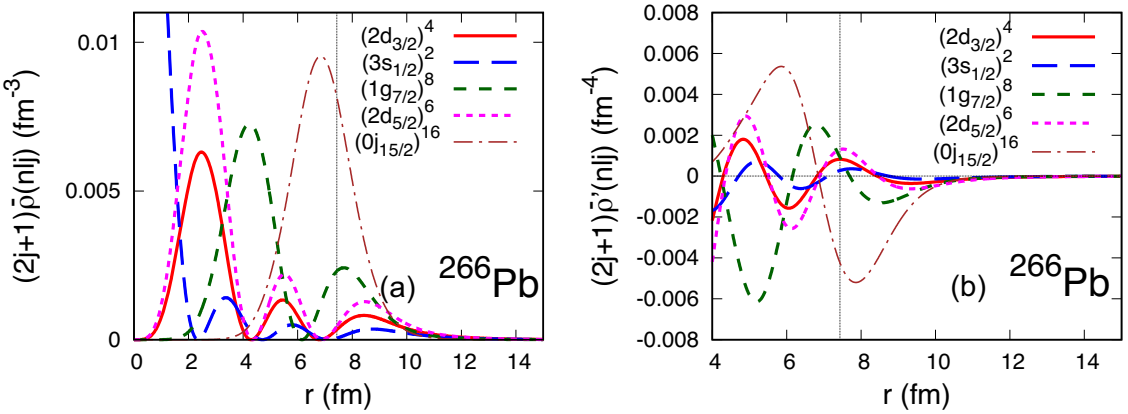

Fig. 13. Same as Fig. 8 but for ^{266}Pb. Vertical lines indicate the radius parameter $R = 7.43$ fm. Note that the values $r < 4$ are not shown in panel (b) for the sake of visibility.

After the $1g_{9/2}$ orbit is fully occupied, the surface diffuseness decreases at $136 < N \leq 164$ because neutrons occupy the nodeless $0i_{11/2}$ and $0j_{15/2}$ orbits, which have a fast drop-off of the wave function at the radius parameter R. At $N > 164$, the diffuseness parameter is again enhanced by the filling of the nodal s.p. orbits $2d_{5/2}$, $3s_{1/2}$, $1g_{7/2}$, and $2d_{3/2}$ up to $N = 184$. Figure 13 plots the neutron s.p. densities and their derivatives of ^{266}Pb. The occupation of the outermost core (^{246}Pb) orbit, $0j_{15/2}$, forms a sharp nuclear surface but the other 20 nucleons in these $2d_{5/2}$, $3s_{1/2}$, $1g_{7/2}$, $2d_{3/2}$ orbits produce diffused nuclear surface beyond $N = 164$. The l dependence of these nodal s.p. orbits is small. Their individuality is almost lost for such a heavy nucleus.

3.5 *Characteristics of s.p. densities*

Finally, I discuss why the nodal or lower-l s.p. orbits near the Fermi level are important to form a diffused nuclear surface. It is known that the rms radius of the harmonic oscillator (HO) s.p. wave function depends only on the principal quantum number ($q = 2n + l$). The difference appears when a more realistic mean-field potential is considered. The potential in general includes diffused central and surface-type spin-orbit potentials, resulting in the enhancement of

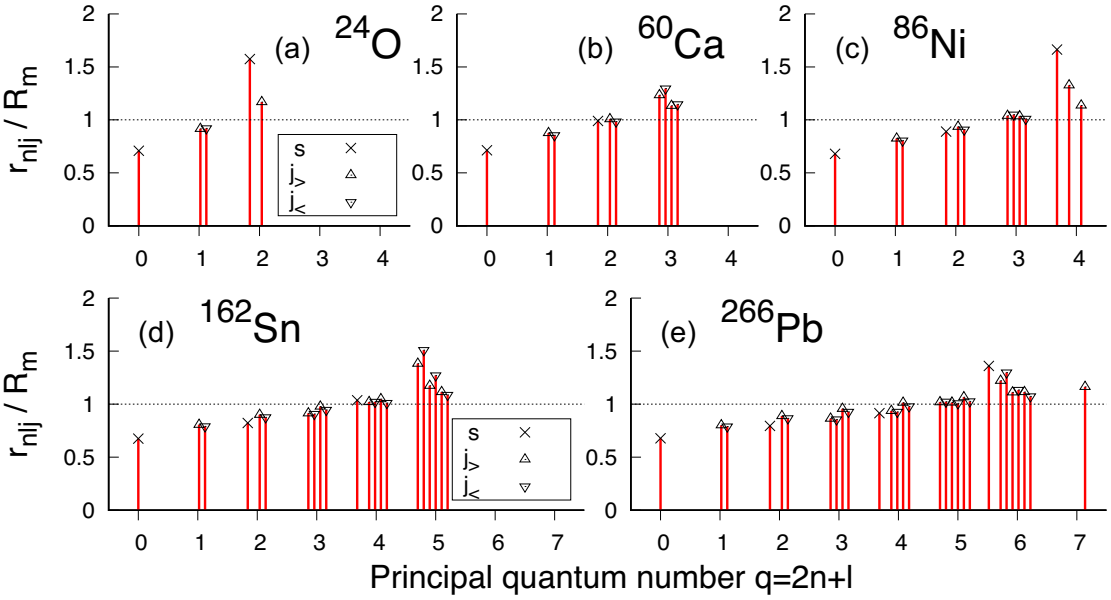

Fig. 14. The rms radius of the neutron s.p. density divided by the rms matter radius categorized into the principal quantum number $2n + l$. Crosses, triangles, and inverted triangles indicate s, $j_> = l + 1/2$, and $j_< = l - 1/2$ orbits, respectively. The values in the same $q = 2n + l$ are arranged from left to right in the order of $j_>$ and $j_<$ from low to high l. Bars are a guide to the eye. Horizontal dotted lines indicate unity.

the amplitude of the s.p. wave functions near the nuclear surface, especially for the s.p. states near the Fermi level.

Figure 14 plots the neutron rms s.p. radii divided by the rms matter radius for the neutron dripline nuclei predicted by the present parameter set, i.e., ^{24}O, ^{60}Ca, ^{86}Ni, ^{162}Sn, and ^{266}Pb, categorized into the principal quantum number $q = 2n + l$. The maximum principal quantum number $q_{\max}$ is 2, 3, 4, 5, and 6–7 for ^{24}O, ^{60}Ca, ^{86}Ni, ^{162}Sn, and ^{266}Pb, respectively. For the sake of convenience, the results with the same q are arranged from left to right in the order of $j_> = l + 1/2$ and $j_< = l - 1/2$ from low to high l, for example, the order of $1s_{1/2}$, $0d_{5/2}$, and $0d_{3/2}$ for $q = 2$; and $1p_{3/2}$, $1p_{1/2}$, $0f_{7/2}$, and $0f_{5/2}$ for $q = 3$.

For deeply bound or "core" orbits $q \leq q_{\max} - 1$ ($q \leq 5$ for ^{266}Pb), the rms s.p. radii are roughly proportional to $q = 2n + l$; i.e., almost constant behavior of the rms neutron s.p. radii is found with respect to l and j at the same major shell as expected from the properties of the HO wave function. Since these deeply bound states have smaller rms radii than the nuclear radius, the $D(nlj)$ value is negative or has at most a small positive value, which does not cause a sudden increase in the surface diffuseness but induces a gradual increase in the surface diffuseness on N. In contrast to this, the rms s.p. radii that belong to the maximum principal quantum number $q_{\max}$ exhibit some angular momentum dependence: The lower the l, the larger the rms s.p. radius becomes. The behavior of the rms neutron radii near the Fermi level can be explained simply by considering the change in the classical turning point on the effective potential well. The lower the l, the larger the rms radius becomes because lower-l orbits have in general more penetrability at the surface region if the binding s.p. energy is the same. For states near the Fermi level, the radius of the classical turning point on the effective potential well becomes larger due to the surface-diffused nuclear potential, leading to a large rms s.p. radius. This also lowers the centrifugal barrier and further increases the rms s.p. radius. The $j_<$ orbit gives a

smaller rms radius than that of the $j_>$ one because the repulsive spin-orbit interaction near the nuclear surface acts opposite to the $j_>$ state.

This non-trivial increase in the rms s.p. radius near the Fermi level is essential to explain the evolution of the nuclear surface diffuseness. In Fig. 14, the rms s.p. radii that belong to $N_{s,\,\mathrm{max}}$, i.e., that exceed the rms matter radius, exceed unity. The $D(nlj)$ value of the nodal s.p. orbits near the Fermi level can be positive, in which the radius parameter R is located before the last peak position, while the $D(nlj)$ value is negative for the nodeless high-l s.p. orbit. Deducing the surface density will be important for detailed study of the nuclear s.p. orbits near the Fermi level. For example, an interesting modification of the s.p. wave functions due to the spin-orbit interaction near the Fermi level was suggested in Ref. [57], which could be essential for explaining the puzzle of the kink structure of the charge radii of Pb isotopes.

4. Conclusion

To extract spectroscopic information from the nuclear surface diffuseness, I have proposed a practical and convenient way to decompose the surface diffuseness into contributions of each single-particle (s.p.) orbit. The nuclear surface diffuseness defined in a familiar two-parameter Fermi density distribution is inversely proportional to the sum of the derivatives of the s.p. wave functions at the nuclear surface radius. I have quantified its contributions to the surface diffuseness for spherical neutron-rich O, Ca, Ni, Sn, and Pb isotopes using a phenomenological mean-field model.

I find that the neutron number dependence of the surface diffuseness can be simply understood by the quantum number of the occupied s.p. orbits near the Fermi level: The occupation of nodeless s.p. orbits induces a mild change in the surface diffuseness, while the occupation of nodal s.p. orbits enhances the surface diffuseness because the nodal s.p. orbit near the Fermi level can have a relatively large s.p. radius that exceeds the matter radius and lowers the orbital angular momentum. The enhancement becomes significant when the neutron dripline is approached where a sudden increase in the s.p. radius near the Fermi level is expected.

The present method can be applied to more realistic nuclear systems that include configuration mixing of spherical s.p. orbits induced by, e.g., nuclear deformation and pairing correlations, if decomposition of their s.p. orbits into spherical s.p. orbits is done. Applying it to these systems, it may be possible to quantitatively show how the density distribution near the nuclear surface is composed microscopically, depending on the degree of these correlations. It should be noted that the surface diffuseness is a robust physical quantity that can be measured by, e.g., proton elastic scattering [15,29,30]. A systematic measurement of the surface diffuseness strongly facilitates the understanding of various phenomena near the nuclear surface.

Acknowledgements

This work was in part supported by JSPS KAKENHI Grant No. 18K03635. I acknowledge the Collaborative Research Program 2021, Information Initiative Center, Hokkaido University.

References

[1] I. Tanihata, H. Hamagaki, O. Hashimoto, Y. Shida, N. Yoshikawa, K. Sugimoto, O. Yamakawa, T. Kobayashi, and N. Takahashi, Phys. Rev. Lett. **55**, 2676 (1985).
[2] A. Ozawa, T. Suzuki, and I. Tanihata, Nucl. Phys. A **693**, 32 (2001).
[3] S. Bagchi et al., Phys. Rev. Lett. **124**, 222504 (2020).
[4] I. Tanihata, H. Savajols, and R. Kanungo, Prog. Part. Nucl. Phys. **68**, 215 (2013).

[5] T. Suzuki et al., Phys. Rev. Lett. **75**, 3241 (1995).
[6] M. Takechi et al., Phys. Lett. B **707**, 357 (2012).
[7] M. Takechi et al., Phys. Rev. C **90**, 061305(R) (2014).
[8] H. de Vries, C. W. de Jager, and C. de Vries, At. Data Nucl. Data Tables **36**, 495 (1987).
[9] S. Terashima et al., Phys. Rev. C **77**, 024317 (2008).
[10] J. Zenihiro et al., Phys. Rev. C **82**, 044611 (2010).
[11] H. Sakaguchi, J. Zenihiro, Prog. Part. Nucl. Phys. **97**, 1 (2017).
[12] K. Tsukada et al., Phys. Rev. Lett. **118**, 262501 (2017).
[13] Y. Matsuda et al., Phys. Rev. C **87**, 034614 (2013).
[14] S. Chebotaryov et al., Prog. Theor. Exp. Phys. **2018**, 053D01 (2018).
[15] S. Hatakeyama, W. Horiuchi, and A. Kohama, Phys. Rev. C **97**, 054607 (2018).
[16] P.-G. Reinhard and W. Nazarewicz, Phys. Rev. C **81**, 051303(R) (2010).
[17] L. W. Chen, C. M. Ko, B. A. Li, and J. Xu, Phys. Rev. C **82**, 024321 (2010).
[18] K. Iida and K. Oyamatsu, Phys. Rev. C **69**, 037301 (2004).
[19] W. Horiuchi, S. Ebata, and K. Iida, Phys. Rev. C **96**, 035804 (2017).
[20] K. Minomo, T. Sumi, M. Kimura, K. Ogata, Y. R. Shimizu, and M. Yahiro, Phys. Rev. C **84**, 034602 (2011).
[21] K. Minomo, T. Sumi, M. Kimura, K. Ogata, Y. R. Shimizu, and M. Yahiro, Phys. Rev. Lett. **108**, 052503 (2012).
[22] T. Sumi, K. Minomo, S. Tagami, M. Kimura, T. Matsumoto, K. Ogata, Y. R. Shimizu, and M. Yahiro, Phys. Rev. C **85**, 064613 (2012).
[23] W. Horiuchi, T. Inakura, T. Nakatsukasa, and Y. Suzuki, Phys. Rev. C **86**, 024614 (2012).
[24] S. Watanabe et al., Phys. Rev. C **89**, 044610 (2014).
[25] W. Horiuchi, T. Inakura, T. Nakatsukasa, and Y. Suzuki, JPS Conf. Proc. **6**, 030079 (2015).
[26] M. Tanaka et al., Phys. Rev. Lett. **124**, 102501 (2020).
[27] W. Horiuchi and T. Inakura, Phys. Rev. C **101**, 061301(R) (2020).
[28] G. Scamps, D. Lacroix, G. G. Adamian, and N. V. Antonenko, Phys. Rev. C **88**, 064327 (2013).
[29] V. Choudhary, W. Horiuchi, M. Kimura, and R. Chatterjee, Phys. Rev. C **102**, 034619 (2020).
[30] V. Choudhary, W. Horiuchi, M. Kimura, and R. Chatterjee, Phys. Rev. C **104**, 054313 (2021).
[31] A. Bohr and B. R. Mottelson, Nuclear Structure (Benjamin, New York, 1975), **Vol. I**.
[32] A. Kohama, K. Iida, and K. Oyamatsu, J. Phys. Soc. Jpn. **85**, 094201 (2016).
[33] S. Mizutori, J. Dobaczewski, G. A. Lalazissis, W. Nazarewicz, and P.-G. Reinhard, Phys. Rev. C **61**, 044326 (2000).
[34] W. Horiuchi, Y. Suzuki, B. Abu-Ibrahim, and A. Kohama, Phys. Rev. C **75**, 044607 (2007).
[35] B. Abu-Ibrahim, S. Iwasaki, W. Horiuchi, A. Kohama, and Y. Suzuki, J. Phys. Soc. Jpn. **78**, 044201 (2009).
[36] M. Langevin et al., Phys. Lett. B **150**, 71 (1985).
[37] D. Guillemaud-Mueller et al., Phys. Rev. C **41**, 937 (1990).
[38] O. Tarasov et al., Phys. Lett. B **409**, 64 (1997).
[39] J. Meng, H. Toki, J. Y. Zeng, S. Q. Zhang, and S.-G. Zhou, Phys. Rev. C **65**, 041302(R) (2002).
[40] G. Hagen, M. Hjorth-Jensen, G. R. Jansen, R. Machleidt, and T. Papenbrock, Phys. Rev. Lett. **109**, 032502 (2012).
[41] G. Hagen, P. Hagen, H.-W. Hammer, and L. Platter, Phys. Rev. Lett. **111**, 132501 (2013).
[42] D. Hove, E. Garrido, P. Sarriguren, D. V. Fedorov, H. O. U. Fynbo, A. S. Jensen, and N. T. Zinner, Phys. Rev. Lett. **120**, 052502 (2018).
[43] B. Abu-Ibrahim and Y. Suzuki, Phys. Rev. C **61**, 051601(R) (2000).
[44] R. J. Glauber, in Lectures in Theoretical Physics, eds. W. E. Brittin Brittin and L. G. Dunham Dunham (Interscience, New York, 1959), Vol. **1**, p. 315.
[45] B. Abu-Ibrahim, W. Horiuchi, A. Kohama, and Y. Suzuki, Phys. Rev. C **77**, 034607 (2008); **80**, 029903(E) (2009); **81**, 019901(E) (2010) [errata].
[46] W. Horiuchi and Y. Suzuki, Phys. Rev. C **74**, 034311 (2006).
[47] W. Horiuchi, Y. Suzuki, P. Capel, and D. Baye, Phys. Rev. C **81**, 024606 (2010).
[48] W. Horiuchi, S. Hatakeyama, S. Ebata, and Y. Suzuki, Phys. Rev. C **93**, 044611 (2016).
[49] W. Horiuchi, S. Hatakeyama, S. Ebata, and Y. Suzuki, Phys. Rev. C **96**, 024605 (2017).
[50] T. Nagahisa and W. Horiuchi, Phys. Rev. C **97**, 054614 (2018).
[51] A. Ozawa et al., Nucl. Phys. A **691**, 599 (2001).

[52] L. Chulkov et al., Nucl. Phys. A **603**, 219 (1996).
[53] I. Angeli and K. P. Marinova, At. Data Nucl. Data Tables **99**, 69 (2013).
[54] R. F. Garcia Ruiz et al., Nat. Phys. **12**, 594 (2016).
[55] L. C. Chamon, B. V. Carlson, L. R. Gasques, D. Pereira, C. De Conti, M. A. G. Alvarez, M. S. Hussein, M. A. Cândido Ribeiro, E. S. Rossi, Jr, and C. P. Silva, Phys. Rev. C **66**, 014610 (2002).
[56] W. Horiuchi and T. Inakura, Prog. Theor. Exp. Phys. **2021**, 103D02 (2021).
[57] H. Nakada, Phys. Rev. C **100**, 044310 (2019).